nature COMMUNICATIONS

ARTICLE

https://doi.org/10.1038/s41467-019-10361-3 OPEN

Chemically modified graphene films with tunable negative Poisson's ratios

Yeye Wen[1,5], Enlai Gao[2,5], Zhenxing Hu[3,5], Tingge Xu[3], Hongbing Lu[3], Zhiping Xu[4] & Chun Li[1]

Graphene-derived macroscopic assemblies feature hierarchical nano- and microstructures that provide numerous routes for surface and interfacial functionalization achieving unconventional material properties. We report that the microstructural hierarchy of pristine chemically modified graphene films, featuring wrinkles, delamination of close-packed laminates, their ordered and disordered stacks, renders remarkable negative Poisson's ratios ranging from −0.25 to −0.55. The mechanism proposed is validated by the experimental characterization and theoretical analysis. Based on the understanding of microstructural origins, pre-strech is applied to endow chemically modified graphene films with controlled negative Poisson's ratios. Modulating the wavy textures of the inter-connected network of close-packed laminates in the chemically modified graphene films also yields finely-tuned negative Poisson's ratios. These findings offer the key insights into rational design of films constructed from two-dimensional materials with negative Poisson's ratios and mechanomutable performance.

[1] Department of Chemistry, MOE Key Laboratory of Bioorganic Phosphorus Chemistry & Chemical Biology, Tsinghua University, Beijing 100084, China. [2] Department of Engineering Mechanics, School of Civil Engineering, Wuhan University, Wuhan, Hubei 430072, China. [3] Department of Mechanical Engineering, The University of Texas at Dallas, 800 W. Campbell Rd., Richardson, TX 75080, USA. [4] Applied Mechanics Laboratory, Department of Engineering Mechanics and Center for Nano and Micro Mechanics, Tsinghua University, 100084 Beijing, China. [5] These authors contributed equally: Yeye Wen, Enlai Gao, Zhenxing Hu. Correspondence and requests for materials should be addressed to Z.X. (email: xuzp@tsinghua.edu.cn) or to C.L. (email: chunli@mail.tsinghua.edu.cn)

Macroscopic chemically modified graphene (CMG) films, processed from graphene oxide (GO) or reduced GO (rGO), feature inter-connected two-dimensional (2D) network structures, lightweight, exceptional mechanical properties, as well as high electrical and thermal conductivities[1–3]. These films have been demonstrated for applications ranging from membrane separation[4–8] to flexible energy storage devices[9,10]. Superior mechanical performance of the CMG films is a prerequisite for these applications. Recent studies on the mechanical properties of the CMG films are mainly focused on tensile strength, stiffness, and toughness, but few are on the Poisson's ratio, which is an important material parameter directly related to the modern functional materials[11,12].

The Poisson's ratio (ν) characterizes the transverse deformation induced by uniaxial strain. For an isotropic, linear elastic and homogeneous material, thermodynamics requires ν to fall within $-1 < \nu < 0.5$[13], being from the most extendable to the most incompressible, although the limitation can be broken for anisotropic materials. Under uniaxial tension, most of the common materials contract in lateral directions to compensate for stretch-induced volume change, giving positive Poisson's ratios. Recent studies show that some natural and synthetic materials have a wide range of negative Poisson's ratios (NPRs) exhibiting auxetic behavior[11,12,14–17], which gives rise to such remarkable properties as enhanced toughness, indentation resistance, and shear stiffness. These enhanced mechanical properties allow the materials with notable NPRs to hold great promises for applications in aircraft, automotive, body-armor, and fiber composites with great pull-out resistance[11,12].

The Poisson's ratio of graphene monolayer has been characterized by molecular dynamics simulations[18–22]. Grima et al. discovered that the conformation of graphene can be modified via the introduction of defects (by removing atoms), and the crumpled conformation of graphene results in tunable NPRs, where a "crumpled paper" model was proposed to explain the NPR behavior of graphene[18]. It is also shown that the graphene monolayer exhibits large NPRs in specific directions if defects are introduced in a periodic arrangement, yielding a wavy form of graphene[22]. More recently, Wan et al. reported that the Poisson's ratios of GO monolayer can be effectively tuned by increasing the degree of oxidation in GO, reaching a value of −0.57 for fully oxidized graphene[20]. The dependence of the Poisson's ratio on the level of oxidation is attributed to the tension-induced suppression of ripples resulting from structural distortion, or in other works, through the disorder-related auxetic egg-rack mechanism. A considerable amount of effort has also been devoted to the Poisson's ratio in three-dimensional (3D), bulk graphene assemblies[23,24]. The results indicated that the microstructures of 3D CMG materials play a key role in modulating the Poisson's ratio. However, compared to the graphene and GO monolayers or their 3D bulk assemblies, little is known about the Poisson's effects in macroscopic CMG films.

In this work, we demonstrate that pristine GO and rGO films prepared by vacuum-assisted filtration and evaporation-induced self-assembly methods exhibit tunable NPRs in a wide range from −0.25 to −0.55 by engineering their chemistry and microstructures. Hierarchical structures of CMG films assembled from GO or rGO sheets are responsible for the NPR effect, as revealed by X-ray diffraction (XRD) and polarized Raman analysis. Theoretical model analysis clarifies that stretching induces suppression of the wrinkled close-packed laminates (CPLs), as well as their disordered stacks and delamination, which explains the tunability of NPR behavior in the CMG films. This well-controlled in-plane auxetic behavior, coupled with their lightweight and outstanding mechanical properties, makes CMG films promising for applications in aerospace, automotive, and defense.

Results

Preparation of CMG films. GO sheets were synthesized by the modified Hummers method at oxidation temperatures 0 and 35 °C (labelled as GO_0 and GO_{35}, respectively, Supplementary Note 1)[25,26]. The structural characterization indicates a lower degree of oxidation, a larger graphitic domain, and fewer defects in GO_0 sheets compared to the GO_{35} sheets (Supplementary Note 2 and Supplementary Fig. 1). Evaporation-induced assembly of concentrated GO dispersions (5 mg mL^{-1}) on a flat substrate or vacuum-assisted filtration of dilute GO dispersions (1 mg mL^{-1}) yields robust and uniform GO films, which could be easily peeled off from the substrate or membrane (Supplementary Fig. 2). All rGO films were obtained by post-reduction of relevant GO films with HI solution. For clarity, the abbreviation x-GO_y is used to indicate the specimens, where x represents the film-forming methods used (e for evaporation and f for filtration) and y represents the oxidation temperature (0 for 0 °C with optimized intact structure[25] and 35 for 35 °C by the conventional procedure[26]). Specially, x-GO or GO_y is used to represent GO samples with one specific characteristic. Thermal gravimetric analysis (TGA) shows that the solvent entrapped in the film does not depend on the fabrication methods. All CMG films feature smooth surfaces, laminated microstructures, and excellent mechanical properties as reported previously (Supplementary Note 3 and Supplementary Figs. 2 and 3)[1,3].

Measurements of Poisson's ratios. A Poisson's ratio is defined as the negative ratio of the transverse strain to the longitudinal strain in the loading direction under uniaxial tension. Thus, accurate determination of the local transverse strain within the region of uniform deformation and avoiding gripping effect in measuring longitudinal strain of a specimen proposed in our previous work[27] are prerequisites for evaluating the Poisson's ratio accurately, and the measurement of Poisson's ratio on a film specimen remains challenging. Herein, fluorescent digital image correlation (FDIC) is used to measure the in-plane deformation by tracking and matching a distinct speckle pattern in the reference and the deformed images during the loading process[28,29]. This approach allows measurement of the full-field displacements with sub-pixel accuracy. Fluorescent particles are used to form speckle patterns to keep track of movement of material points in the film under deformation. This approach eliminates the light specular reflection (Fig. 1a). Typical FDIC speckle images of e-GO_0 film are shown in Fig. 1b–e, where X and Y are the transverse and loading directions, U and V are the corresponding displacement fields along the X and Y directions, respectively. The results show that the strains along the transverse and loading directions (ε_{xx} and ε_{yy}) of the GO film are both positive, and the average transverse strain increases with the increase of average longitudinal strain, signaling a NPR behavior. Based on the transverse strain ε_X and longitudinal strain ε_Y averaged from the strain fields ε_{xx} and ε_{yy} (Fig. 2a and Supplementary Fig. 4), the instantaneous in-plane Poisson's ratio is calculated as:

$$\nu_{YX} = -\mathrm{d}\varepsilon_X/\mathrm{d}\varepsilon_Y \quad (1)$$

As shown in Fig. 2a, upon uniaxial loading along the Y direction for e-GO_0 film, the ε_X increases linearly with ε_Y, giving an instantaneous Poisson's ratio around a constant value of −0.47, which is independent of the applied longitudinal strain (Fig. 2b). Impressively, it is found that all the examined GO and rGO films exhibit NPR behavior (Supplementary Fig. 4), irrespective of the GO precursors used, film-forming methods, and the chemical structure of CMG (GO or rGO) sheets. The

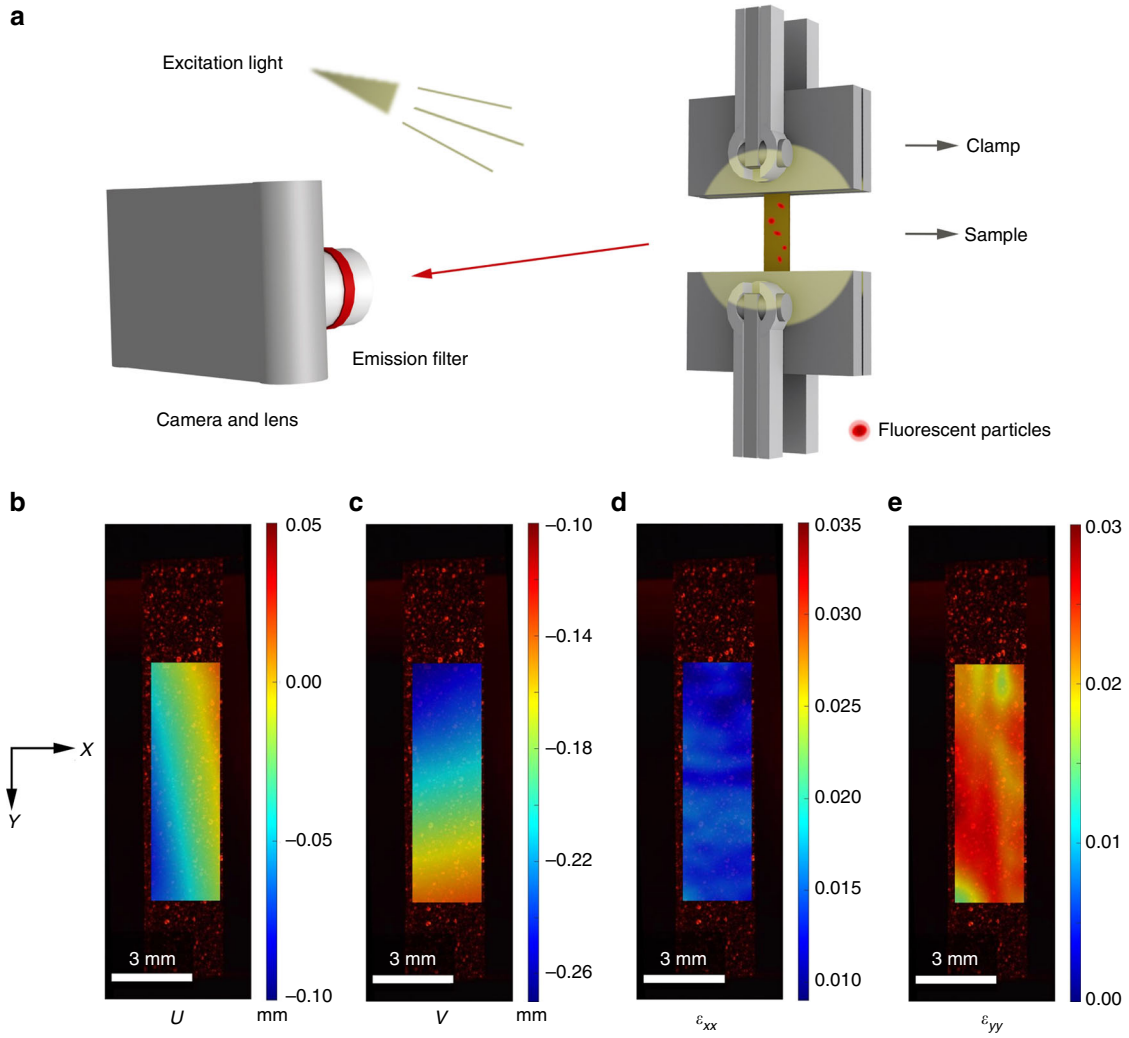

Fig. 1 Tensile tests of chemically modified graphene films monitored by fluorescent digital image correlation. **a** Schematic diagram of the fluorescent digital image correlation (FDIC) measurement, where camera and lens detect light emitted from red fluorescent particles deposited onto the e-GO_0 films (prepared by evaporation of GO solution synthesized at 0 °C). The emission filter allows only light from the excited fluorescent particles to pass. **b**–**e** Optical images of e-GO_0 films with fluorescent particles on its surface, and the displacement fields *U* (**b**) and *V* (**c**), and the strain fields measured in the transverse (**d**) and longitudinal (**e**) directions from FDIC analysis. Source data are provided as a Source Data file

average Poisson's ratios for the films are determined as −0.26 (*e*-GO_{35}), −0.25 (*f*-GO_{35}), −0.44 (*f*-GO_0), −0.48 (*f*-rGO_0), −0.53 (*e*-GO_0), and −0.55 (*e*-rGO_0) (Fig. 2c), via Eq. (1) using the full range of data (Supplementary Fig. 4). Moreover, cyclic loads with a peak strain of 1.5% does not induce significant changes in the Poisson's ratio even after 15 cycles (Fig. 2d and Supplementary Fig. 5), indicating that the NPR effect is inherent for the CMG films.

Microstructural basis of the negative Poisson's effects. The chemical structures of GO building blocks modulate the microstructures and Poisson's ratio of the GO films. As shown in Fig. 3a, all XRD patterns of GO_0 and GO_{35} films display sharp diffraction peaks, suggesting the formation of CPLs, which is evident from the scanning electron microscopy (SEM) images of CMG films (Supplementary Fig. 2b)[1]. The interlayer spacings of *e*-GO_0 and *f*-GO_0 films are calculated as 0.806 and 0.785 nm, respectively, based on the diffraction peaks at $2\theta = 10.95°$ and 11.25° with the full-width at half-maximum (FWHM) of 1.23° and 1.05°. *e*-GO_{35} and *f*-GO_{35} films feature smaller interlayer spacings of 0.772 and 0.750 nm, respectively, which are determined from diffraction peaks at higher angles $2\theta = 11.44°$ and 11.77° with narrower FWHMs (0.56° and 0.47°). The XRD data can be used to evaluate the degree of disorder of GO sheets in the CMG films, where the finite FWHM indicates the sheet mis-alignment[30,31]. It is distinct that the GO_0 films with larger FWHM have larger absolute values of NPRs (−0.53 (*e*-GO_0) and −0.44 (*f*-GO_0)) than GO_{35} films (−0.26 (*e*-GO_{35}) and −0.25 (*f*-GO_{35})). The increased amount of organosulfate (3.33 at% sulfur) in GO_0 films relative to that (0.77 at%) in GO_{35} films is suggested to account for the larger *d*-spacing and less ordered alignment of GO_0 films[26,32]. The interlayer spacing between GO sheets characterized by XRD measures the packing density in CPLs, which is high enough to suppress the out-of-plane corrugation at the sheet level, which was proposed to be responsible for the NPR effects of graphene and GO monolayers[18–22].

The structural differences between the GO sheets prepared by different synthetic protocols are further identified by UV–vis absorption spectra. The main absorption peak of GO around 230 nm is associated with the sp^2 domain in GO sheets. The absorption peak of GO_0 (236 nm) is red-shifted with respect to that of GO_{35} (231 nm), demonstrating that GO_0 sheets have a larger graphitic domain than that in GO_{35}, since the carbon atom

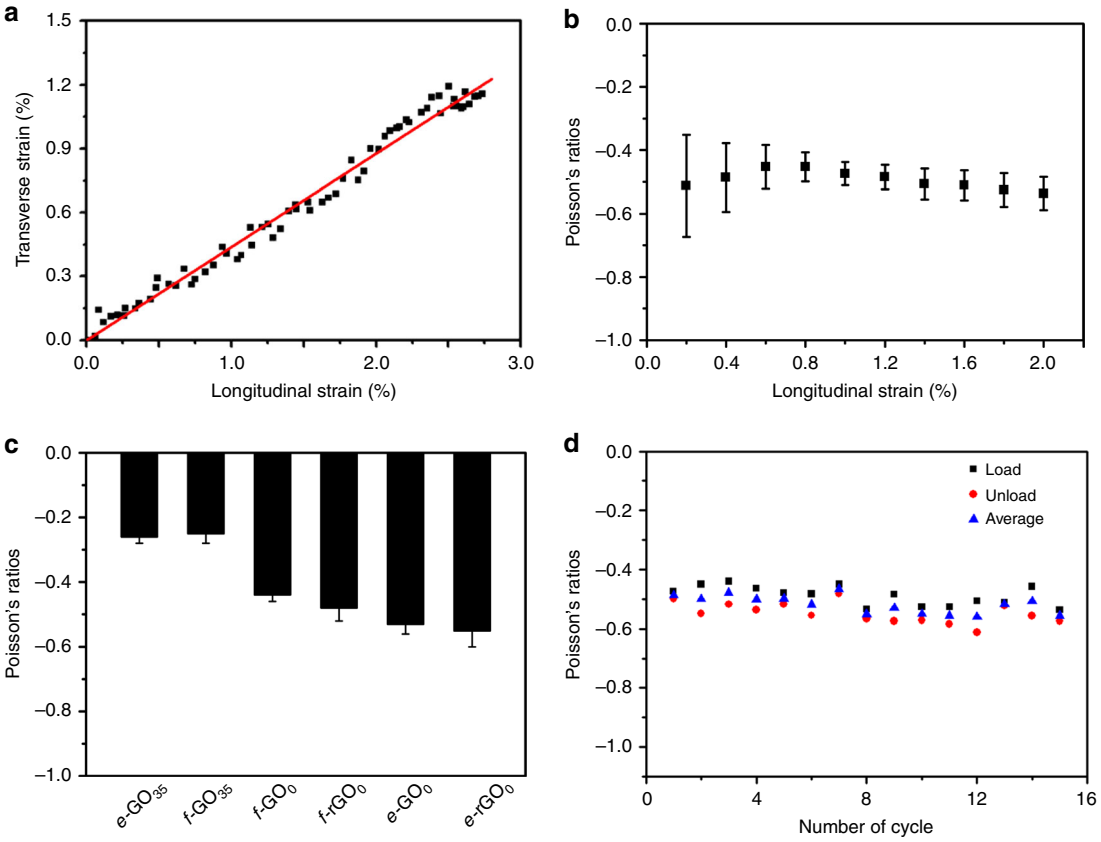

Fig. 2 Typical mechanical response of chemically modified graphene films. **a** The transverse strain ε_X plotted as a function of the longitudinal strain ε_Y of e-GO_0 films under a tensile loading in the *Y* direction. The red line is the linear fitting line. **b** The instantaneous Poisson's ratios of e-GO_0 films averaged from three samples in Fig. S4b. **c** Poisson's ratios of e-GO_{35} films (prepared by evaporation of GO solution synthesized at 35 °C), *f*-GO_{35} (prepared by filtration of GO solution synthesized at 35 °C), *f*-GO_0 (prepared by filtration of GO solution synthesized at 0 °C), *f*-rGO_0 (reduced *f*-GO_0 films), e-GO_0 and e-rGO_0 (reduced e-GO_0 films). **d** Poisson's ratios of e-GO_0 films under cyclic uniaxial tensile loading with a peak strain of 1.5%. The error bars in panels (**b**, **c**) indicate the standard errors (three samples were measured). Source data are provided as a Source Data file

rupture is prevented to some extent by a relatively lower temperature of oxidization (Supplementary Fig. 6)[33,34]. The low defect density and larger sp^2 domains within GO_0 basal planes facilitate the van der Waals interactions between neighboring GO_0 sheets[34,35]. Consequently, in film-forming processes by evaporation-induced assembly or vacuum-assisted filtration, the mobility of GO_0 sheets in the dispersions is limited, and it becomes difficult to adjust the sheet conformation to adopt an energetically-favorable, ordered alignment, resulting in the formation of GO_0 films, where the hierarchical structures of GO sheet-containing CPLs is less ordered compared with GO_{35} films.

The Poisson's ratio of the CMG films depends on the film microstructures tailored by the film-forming methods. As seen in Fig. 3a, with the same GO precursors, evaporation-induced assembly of concentrated GO dispersion (5 mg mL^{-1}) produces *e*-GO films with larger interlayer spacing and FWHM, together with more significant NPR effects than the *f*-GO films fabricated by vacuum-assisted filtration from dilute GO dispersions (1 mg mL^{-1}). GO sheets intend to form a low-density dynamic network at a relatively higher concentration (≥3 mg mL^{-1}) due to the presence of strong physical cross-linking sites[26,36], leading to the formation of CMG films with more wrinkled textures of the CPLs. Considering all of these factors, we conclude that the Poisson's ratio of CMG films is highly related to the topological structure of CPLs, which can be modulated by the chemical structures of GO building blocks and the film-forming methods. The wrinkled textures of CPLs enhance the NPR effect of the CMG films. After reduction with hydroiodic acid solution, the rGO films feature similar hierarchical structures with wrinkled textures and the associated auxetic behavior exhibited in the GO films (Fig. 2c and Supplementary Fig. 2).

To gain further insights into the NPR behavior of GO films, *e*-GO_0 films with different orders of alignment of CPLs were prepared by pre-stretching the wet GO films during the film-forming process. It is found that upon increasing the load, the resultant *e*-GO_0 films exhibit smaller absolute values of NPRs and narrower FWHMs, ranging from $\nu = -0.53$ (FWHM = 1.23°, without pre-stretch) to $\nu = -0.46$ (FWHM = 1.13°, with 30 mN pre-stretch), and $\nu = -0.31$ (FWHM = 1.04°, with 60 mN pre-stretch) (Fig. 3b and Supplementary Figs. 7 and 8). Consequently, pre-stretch induces conformation changes of the CPLs in the CMG films, which are gradually aligned to a more energetically-favorable arrangement at the expense of forming wrinkled textures. These results demonstrate that the NPR behavior of the CMG films can be readily tuned by controlling the topological structure of CPLs and their stacks in the films. This observation has also been confirmed by polarized Raman spectral examinations of CMG films prepared under different amplitudes of pre-stretch.

Polarized Raman spectra were recorded by directing an incident laser beam parallel to the base plane of *e*-GO_0 films with pre-stretch. As shown in Fig. 3c, α is the average angle of alignment between the CPLs and the loading direction, and β is the angle between the electric field vector of the incident laser and the base plane of the *e*-GO_0 film, which is tuned from 0° to 360°

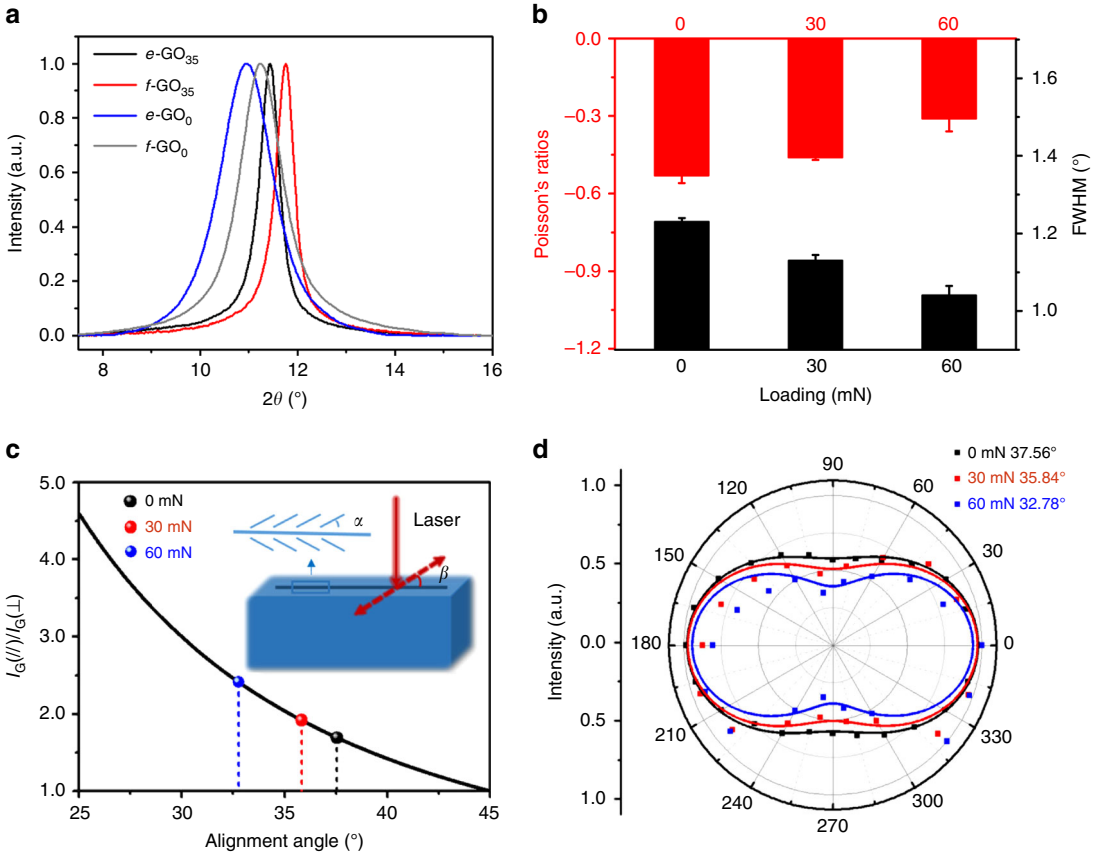

Fig. 3 Microstructural origins of the negative Poisson's ratio (NPR) effect. **a** X-ray diffraction patterns of the e-GO_{35}, f-GO_{35}, e-GO_0, and f-GO_0 films. **b** Poisson's ratios and the full-width at half-maximum (FWHM) measured for the e-GO_0 films under different amplitudes of pre-stretch. **c** Relationship between the value of $I_G(//)/I_G(\perp)$ and the angle of sheet (α) in the films (inset: the polarized Raman setup). **d** The G band intensity, $I_G(\beta)$, plotted as a function of β. Black dots and lines are the experimental data of e-GO_0 films without pre-stretch and the fitting curve using Eq. (2), while the red (blue) ones are the data and fitting curve for e-GO_0 films under 30 (60) mN pre-stretch. The error bars in panel (**b**) indicate the standard errors (three samples for the Poisson's ratios and four samples for FWHM). Source data are provided as a Source Data file

(Supplementary Fig. 9). The G band intensity in polarized Raman spectra of the CMG films is plotted against the angles α and β in Fig. 3d, which follow the equation:

$$I_G = \frac{c^2}{2}\cos^2\alpha\{2 + \cos[2(\alpha-\beta)] + \cos[2(\alpha+\beta)]\} \quad (2)$$

For samples with the angle of alignment α, the value of $I_G(\beta)$ characterized experimentally reaches a maximum at $\beta = 0°$ and 180° ($I_G(//)$), whereas $I_G(\beta)$ reaches a minimum at $\beta = 90°$ and 270° ($I_G(\perp)$)[37]. The ratio $I_G(//)/I_G(\perp)$ equals $\cot^2\alpha$ (Fig. 3c). Fitting the data of normalized Raman G band intensity with the value of β between 0° and 360° using Eq. (2), one obtains the value of α decreasing from 37.56° to 35.84°, and 32.78° upon enhancing pre-stretch (Fig. 3c, d). Based on these results, it becomes clear that the NPR of CMG films can be tuned by modifying their hierarchical microstructures, where the inter-connected network of CPLs define the NPR behavior of the CMG films.

Theoretical analysis. To understand the microstructural evolution of CMG films under tensile loading and quantifying the NPR behavior, we constructed a multiscale model for the CMG films based on experimental evidence. Specifically, based on SEM and optical images of the cross-section and surface topography of the CMG films, respectively (Fig. 4a, b), we illustrated the microstructures of monolithic CMG films in Fig. 4c, which include inter-connected CPLs (or GO multilayers with typical thickness of ~10–40 nm). Their evolution under tensile loading involves aligning of disordered stacks of CPLs, reduction in the out-of-plane corrugation of wrinkled CPLs and their delamination. These processes are activated along the tensile direction, but the misalignment in other directions is also suppressed, as a consequence, endowing the CMG films with NPRs (Fig. 4c). The evidence of these processes can be found from the polarized Raman data. Compared with the flattening process of a GO or graphene monolayer[20], the out-of-plane corrugation of the inter-connected network of CPLs in the CMG film is stabilized by its microstructural hierarchy, and can have much higher amplitude, leading to more prominent NPR effects as we identified experimentally. With these arguments, we rationalize the mechanisms through a representative volume element (RVE) featuring wavy textures of CPLs (Fig. 4d), following the spirit of the model of foldable structures proposed by Grima et al.[38] and the cubic lattice model coined by Baughman and co-workers[39]. In our model, the sticks (solid and dash lines in Fig. 4d) represent the out-of-plane corrugation of CPLs resulted from disordered stacks, wrinkles, or delamination. The angle θ between the sticks and the basal plane of a CMG film measures the out-of-plane corrugation of CPLs, and is related to the alignment angle α measured in polarized Raman experiments (see Supplementary Note 4 for details). The ν–α relation predicted from our model aligns well with experimental data (Fig. 4e), suggesting that the NPR effect of CMG films does originate from the wavy texture of the inter-connected CPL network and will be reduced if the alignment of CPLs improves.

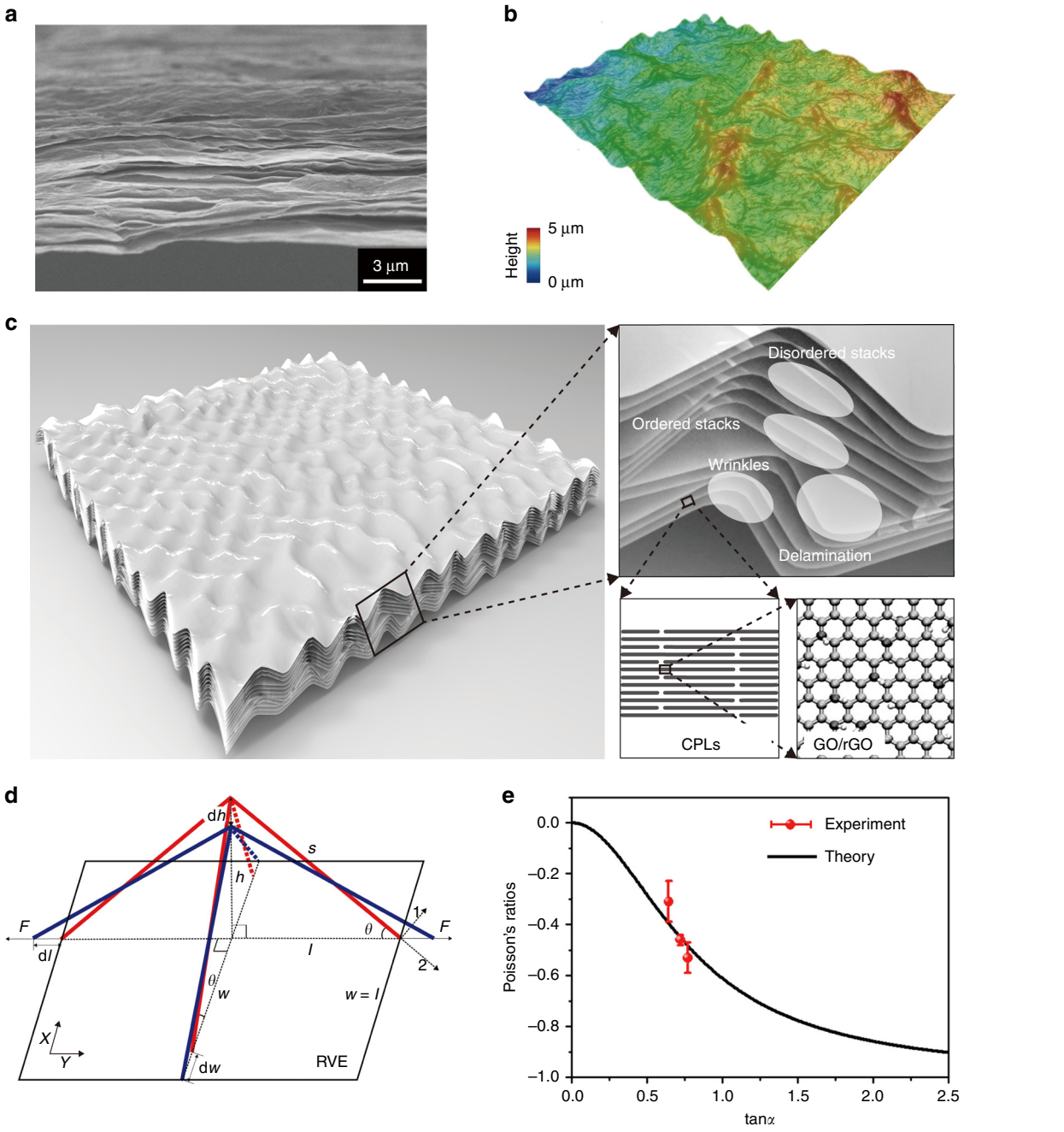

Fig. 4 Mechanisms of negative Poisson ratio (NPR) behaviors explained by the theoretical model. **a** Wrinkles, delamination of close-packed laminates (CPLs) and their ordered, disordered stacks in *e*-GO_0 films characterized by scanning electron microscopy (SEM). **b** Three-dimensional reconstruction of the surface topography of *e*-GO_0 films through optical microscopy. **c** Illustration of the multiscale hierarchical microstructure of a chemically modified graphene (CMG) film featuring individual graphene sheets as the fundamental building blocks, CPLs and their inter-connected network. **d** A 4-stick representative volume element (RVE) model, where the red configuration is stretched by force *F* to the blue one. **e** Theoretical predictions and experimental measurements of the Poisson's ratio as a function of the angle of alignment between CPLs, α, which is related to the value of θ in the model (see Supplementary Note 4 for details). The error bars for experimental data in panel (**e**) indicate the standard errors (three samples were measured). Source data are provided as a Source Data file

Discussion

We have demonstrated that the CMG films fabricated by solution-processed approaches feature NPRs with the value of v ranging from −0.25 to −0.55. It should be noted that the in-plane and out-of-plane microstructures of CMG films are strongly anisotropic. The aligning process of CPLs only results in in-plane NPR effects, while the Poisson's ratio measured in the out-of-plane direction is always positive, with a reduction in the thickness of CMG films by ~20% at a tensile strain of 3.5% as reported in our previous work[27].

Our hypothesis on the microstructural evolution in CMG films is limited by the resolution of structural characterization techniques. Relative sliding between CPLs is not considered, which may weaken the suppression of out-of-plane corrugations of CPLs under tensile loading, and thus reduce the NPR effect. The morphological changes of GO sheets in the CPLs are expected to be strongly constrained by the layer-by-layer packing. The chemical structures of GO sheets are thus correlated to the NPR behaviors through their modulation in the film-forming processes.

Future work on the characteristic microstructural features and their statistics from experimental measurements is required to extract the key parameters for constructing numerical models, which can extend the current analysis by considering more realistic models. Our RVE-based theory neglects the wide distribution of the microstructural features resulted from the coarse control of film preparation processes, but captures the most essential mechanism of the NPR effect by introducing the concept of CPLs. Our experimental characterization and analysis indicate that the wavy textures of close-packed GO laminates as the building blocks are responsible for the observed auxetic behavior in the macroscopic GO and rGO films. The argument is validated by further engineering control of the NPR behaviors. The wrinkled texture of the inter-connected CPL network within the films is readily tailored by the chemical structures of the GO precursors and the film-forming methods, resulting in films with tunable NPR values.

The microstructural hierarchy of CMG films featuring graphene sheets as the building blocks, the CPLs and their interconnected networks is reminiscent of the three-level model of carbon nanotube fibers (individual nanotubes as building blocks, the close-packed bundles, and their inter-connected network)[40]. These abstracted concepts help to improve understanding of the multiscale nature of nanostructured assemblies, their evolution under mechanical loading, and their impacts on the macroscopic mechanical performance[41]. The current study thus furnishes design guidelines for the construction of films with NPR behaviors from 2D building blocks for exhibiting auxetics.

Methods

Preparation of the GO and rGO films. Evaporation-induced assembly of GO_0 or GO_{35} dispersions on a polystyrene Petri dish under ambient condition yield *e*-GO films, which can be easily peeled off from the substrate for further characterization. The evaporation process typically takes 3 days at 25 °C. *f*-GO films were fabricated by vacuum-assisted filtration of dilute GO dispersion (1 mg mL^{-1}) through a poly-(tetrafluoride ethylene) (PTFE) membrane (47 mm in diameter, 0.22 μm pore size). All rGO films were prepared by chemical reduction of the relevant GO films with a mixed ethanol/aqueous 57% HI solution (3/1 by volume) at room temperature for 12 h. The resulting rGO films were repeatedly washed by ample ethanol and dried at room temperature for 24 h before characterizations. Pre-stretched GO films were prepared by sandwiching GO rectangular strips (3 mm × 30 mm) in a home-made apparatus with a given loading under 100% relative humidity (RH) for 1 week, followed by air-drying the resultant GO films under 50% RH for 1 day. The GO strips were fabricated by razor blade cutting wet GO films, which were fabricated by cast-drying GO dispersions (5 mg mL^{-1}) on PTFE Petri dish under 50% RH for 2 days.

Microscopic observations. SEM images were recorded using a Sirion 200 field emission SEM. The samples used for size distribution statistics by SEM were fabricated by deposition of diluted GO solution (5–10 μg mL^{-1}) on a 300-nm-thick-SiO_2/Si wafer followed by drying in a clean bench without sputter-coating any conductive layers. Surface morphology of *e*-GO_0 films was recorded and reconstructed using a 3D optical microscope (KH-8700 HIROX, 2500X).

Structure characterizations. X-ray photoelectron spectroscopy (XPS) data was recorded on an ESCALAB 250 photoelectron spectrometer (ThermoFisher Scientific) with Al Kα (1486.6 eV) radiation. XRD patterns of the films were collected on D8 Advanced X-ray diffractometer with Cu Kα radiation ($\lambda = 0.15418$ nm, Bruker, Germany) with scanning speed of 5° per minute at room temperature. Raman spectra were collected on LabRAMHR instrument (Horiba Jobin Yvon) with a 532-nm wavelength laser. During the polarized Raman characterization of CMG films, the polarization state of laser was tuned by the half-wave plate positioned in the beam path, and a man-made stage was used to vary the angle of film according to the original direction of linearly polarized excitation.

Mechanical characterizations. All samples for tensile testing were cut into rectangular strips with width of 3 mm and length of 30 mm by a single-edge razor blade and attached to a frame of card paper by epoxy glue. Uniaxial tension of the GO and rGO films was carried out using an Instron 3342 universal testing machine (Instron, USA). The transverse strain was determined using an optical microscope to record the videos of the fluorescent particle movement on the film surface at a strain rate of $5 \times 10^{-4}\ s^{-1}$ until the film broke. FDIC was used to track and match the fluorescent patterns in the reference and deformed states. Red fluorescent particles (580/605, Life Technology Corp., #F13083) were used in the fluorescent microscope, with excitation and emission/barrier filters for fluorescent imaging. The primary function of the emission/barrier filter in the fluorescent microscope is to block the excitation wavelengths used and allow only the excited light from the fluorescent particles to pass. Matching filters were thus used for fluorescent imaging (ET560/40x and ET615/40m, Chroma Technology Corp.). The samples were randomly sprayed with fluorescent particles using an airbrush. It should be noted that the displacement measurement in FDIC is sensitive to the sample alignment, and errors may arise from sample gripping. However, for our FDIC data, the angle of misalignment is ~5°, corresponding to an error in the strain of ~0.001. The FDIC-calculated strain is an order of magnitude higher than this level of error, and thus the strain measurement is reliable.

Data availability

The data sets within the article and Supplementary Information of the current study are available from the authors upon request. The source data underlying Figs. 2, 3, and 4e and Supplementary Figs. 1b, c, e, f, 3–9 are provided as a Source Data file.

Received: 2 November 2018 Accepted: 8 May 2019
Published online: 04 June 2019

References

1. Dikin, D. A. et al. Preparation and characterization of graphene oxide paper. *Nature* **448**, 457–460 (2007).
2. Peng, L. et al. Ultrahigh thermal conductive yet superflexible graphene films. *Adv. Mater.* **29**, 1700589 (2017).
3. Wen, Y. Y., Wu, M. M., Zhang, M., Li, C. & Shi, G. Q. Topological design of ultrastrong and highly conductive graphene films. *Adv. Mater.* **29**, 1702831 (2017).
4. Sun, M. & Li, J. H. Graphene oxide membranes: functional structures, preparation and environmental applications. *Nano Today* **20**, 121–137 (2018).
5. Joshi, R. K. et al. Precise and ultrafast molecular sieving through graphene oxide membranes. *Science* **343**, 752–754 (2014).
6. Chen, L. D. et al. Ion sieving in graphene oxide membranes via cationic control of interlayer spacing. *Nature* **550**, 380–383 (2017).
7. Gao, E. L. & Xu, Z. P. Bio-inspired graphene-derived membranes with strain-controlled interlayer spacing. *Nanoscale* **10**, 8585–8590 (2018).
8. Koenig, S. P., Wang, L. D., Pellegrino, J. & Bunch, S. Selective molecular sieving through porous graphene. *Nat. Nanotechnol.* **7**, 728–732 (2012).
9. Liu, Y. Q., He, K., Chen, G., Leow, W. R. & Chen, X. Nature-inspired structural materials for flexible electronic devices. *Chem. Rev.* **117**, 12893–12941 (2017).
10. Lv, T., Liu, M. X., Zhu, D. Z., Gan, L. H. & Chen, T. Nanoarbon-based materials for flexible all-solid-state supercapacitors. *Adv. Mater.* **30**, 1705489 (2018).
11. Greaves, G. N., Greer, A. L., Lakes, R. S. & Rouxel, T. Poisson's ratio and modern materials. *Nat. Mater.* **10**, 823–837 (2011).
12. Huang, C. W. & Chen, L. Negative Poisson's ratio in modern functional materials. *Adv. Mater.* **28**, 8079–8096 (2016).
13. Kosevich, A. M., Lifshitz, E. M., Landau, L. D. & Pitaevskii, L. P. *Theory of Elasticity*. 3rd edn (Butterworth-Heinemann, Washington, DC, 1986).
14. Hall, L. J. et al. Sign change of Poisson's ratio for carbon nanotube sheets. *Science* **320**, 504–507 (2008).
15. Song, F., Zhou, J. B., Xu, X. H., Xu, Y. & Bai, Y. L. Effect of a negative Poisson ratio in the tension of ceramics. *Phys. Rev. Lett.* **100**, 245502 (2008).
16. Jiang, J. W. & Park, H. S. Negative Poisson's ratio in single-layer black phosphorus. *Nat. Commun.* **5**, 4727 (2014).
17. Hewage, T. A. M., Alderson, K. L., Alderson, A. & Scarpa, F. Double-negative mechanical metamaterials displaying simultaneous negative stiffness and negative Poisson's ratio properties. *Adv. Mater.* **28**, 10323–10332 (2016).
18. Grima, J. N. et al. Tailoring graphene to achieve negative Poisson's ratio properties. *Adv. Mater.* **27**, 1455–1459 (2015).
19. Jiang, J. W. & Park, H. S. Negative Poisson's ratio in single-layer graphene ribbons. *Nano Lett.* **16**, 2657–2662 (2016).
20. Wan, J., Jiang, J. W. & Park, H. S. Negative Poisson's ratio in graphene oxide. *Nanoscale* **9**, 4007–4012 (2017).
21. Qin, H. S., Sun, Y., Liu, J. Z., Li, M. J. & Liu, Y. L. Negative Poisson's ratio in rippled graphene. *Nanoscale* **9**, 4135–4142 (2017).
22. Grima, J. N., Grech, M. C., Grima-Cornish, J. N., Gatt, R. & Attard, D. Giant auxetic behaviour in engineered graphene. *Ann. Phys.* **530**, 1700330 (2018).
23. Wu, Y. P. et al. Three-dimensionally bonded spongy graphene material with super compressive elasticity and near-zero Poisson's ratio. *Nat. Commun.* **6**, 6141 (2015).

24. Xu, X. et al. Naturally dried graphene aerogels with superelasticity and tunable Poisson's ratio. *Adv. Mater.* **28**, 9223–9230 (2016).
25. Eigler, S. et al. Wet chemical synthesis of graphene. *Adv. Mater.* **25**, 3583–3587 (2013).
26. Zhang, M. et al. Multifunctional pristine chemically modified graphene films as strong as stainless steel. *Adv. Mater.* **27**, 6708–6713 (2015).
27. Gao, E. L., Wen, Y. Y., Yuan, Y. N., Li, C. & Xu, Z. P. Intrinsic mechanical properties of graphene oxide films: strain characterization and the gripping effects. *Carbon* **118**, 467–474 (2017).
28. Berfield, T. A. et al. Fluorescent image correlation for nanoscale deformation measurements. *Small* **2**, 631–635 (2006).
29. Hu, Z. X., Xu, T. G., Luo, H. Y., Gan, R. Z. & Lu, H. B. Measurement of thickness and profile of a transparent material using fluorescent stereo microscopy. *Opt. Express* **24**, 29822–29829 (2016).
30. Hu, K. S. et al. Written-in conductive patterns on robust graphene oxide biopaper by electrochemical microstamping. *Angew. Chem. Int. Ed.* **52**, 13784–13788 (2013).
31. Zhang, M., Huang, L., Chen, J., Li, C. & Shi, G. Q. Ultratough, ultrastrong, and highly conductive graphene films with arbitrary sizes. *Adv. Mater.* **26**, 7588–7592 (2014).
32. Eigler, S., Grimm, S., Hof, F. & Hirsch, A. Graphene oxide: a stable carbon framework for functionalization. *J. Mater. Chem. A* **1**, 11559–11562 (2013).
33. Kumar, P. V. et al. Scalable enhancement of graphene oxide properties by thermally driven phase transformation. *Nat. Chem.* **6**, 151–158 (2014).
34. Chen, H. W., Wu, M. M. & Li, C. Structural integrity versus lateral size: enhancing graphene-based film materials by reducing planar defects rather than flake boundary. *Carbon* **139**, 216–225 (2018).
35. Liu, Y. L., Xie, B., Zhang, Z., Zheng, Q. S. & Xu, Z. P. Mechanical properties of graphene papers. *J. Mech. Phys. Solids* **60**, 591–605 (2012).
36. Bai, H., Li, C., Wang, X. L. & Shi, G. Q. On the gelation of graphene oxide. *J. Phys. Chem. C* **115**, 5545–5551 (2011).
37. Dai, Z. H. et al. Hierarchical graphene-based films with dynamic self-stiffening for biomimetic artificial muscle. *Adv. Funct. Mater.* **26**, 7003–7010 (2016).
38. Grima, J. N. et al. Modelling and testing of a foldable macrostructure exhibiting auxetic behaviour. *Phys. Status Solidi B* **248**, 117–122 (2011).
39. Baughman, R. H., Shacklette, J. M., Zakhidov, A. A. & Stafstrom, S. Negative Poisson's ratios as a common feature of cubic metals. *Nature* **392**, 362–365 (1998).
40. Gao, E. L., Lu, W. B. & Xu, Z. P. Strength loss of carbon nanotube fibers explained in a three-level hierarchical model. *Carbon* **138**, 134–142 (2018).
41. Xu, Z. P. & Zheng, Q. S. Micro- and nano-mechanics in China: a brief review of recent progress and perspectives. *Sci. China Phys. Mech. Astron.* **61**, 074601 (2018).

Acknowledgements

Y.W. and C.L. are supported by National Natural Science Foundation of China (51673108 and 51433005) and National Key R&D Program of China (2016YFA0200202). Z.X. acknowledges National Natural Science Foundation of China through Grants 11825203 and 11472150. E.G. acknowledges the support from the starting-up fund of Wuhan University and the Fundamental Research Funds for the Central Universities. Z.H., T.X. and H.L. are supported through Grants NSF CMMI-1636306, CMMI-1661246, and CMMI-1726435, and Louis A. Beecherl Jr. Chair. The authors also thank Prof. Gaoquan Shi for discussion and his valuable advices on this work.

Author contributions

C.L. and Z.X. conceived the idea and directed the project. Y.W. carried out materials synthesis, performed materials characterization, and related data analysis. Z.H., T.X. and H.L. offered FDIC methods and equipment for the mechanical tests. Y.W., E.G. and Z.H. measured the Poisson's ratio. Y.W. and E.G. analyzed the data of Poisson's ratios. E.G. developed the theoretical model. All authors participated in the interpretation of the data and the writing of the manuscript.

Additional information

Supplementary Information accompanies this paper at https://doi.org/10.1038/s41467-019-10361-3.

Competing interests: The authors declare no competing interests.

Reprints and permission information is available online at http://npg.nature.com/reprintsandpermissions/

Journal peer review information: *Nature Communications* thanks the anonymous reviewers for their contribution to the peer review of this work. Peer reviewer reports are available.

Publisher's note: Springer Nature remains neutral with regard to jurisdictional claims in published maps and institutional affiliations.

Supplementary Information for

Chemically Modified Graphene Films with Tunable Negative Poisson's Ratios

Yeye Wen,[1,*] Enlai Gao,[2,*] Zhenxing Hu,[3,*] Tingge Xu,[3] Hongbing Lu,[3] Zhiping Xu,[4] and Chun Li[1]

[1]Department of Chemistry, MOE Key Laboratory of Bioorganic Phosphorus Chemistry & Chemical Biology, Tsinghua University, Beijing 100084, China

[2]Department of Engineering Mechanics, School of Civil Engineering, Wuhan University, Wuhan, Hubei 430072, China

[3]Department of Mechanical Engineering, the University of Texas at Dallas, 800 W. Campbell Rd. Richardson, TX, 75080, USA

[4]Applied Mechanics Laboratory, Department of Engineering Mechanics and Center for Nano and Micro Mechanics, Tsinghua University, Beijing 100084, China

[*]These authors contributed equally to this work.

Corresponding authors. E-mails: chunli@mail.tsinghua.edu.cn (C.L.), xuzp@tsinghua.edu.cn (Z.X.).

This Supplementary Information Material contains

- Supplementary Notes on *preparation of GO Dispersions*, *structural characterization of GO sheets*, *mechanical characterization*, and *theoretical model*.
- Supplementary Figures 1-9

Supplementary Note 1 – Preparation of GO Dispersions

GO_0 was synthesized by a modified Hummers method from natural graphite at a relatively low oxidation temperature, 0 ^{o}C. Graphite powder (325 mesh, 3.0 g) was dispersed in a concentrated sulfuric acid (70 mL) under stirring with a constant speed of 350 rpm at 0 °C. After stirring for 0.5 h, potassium permanganate (9 g) was added into flask slowly over a period of 2 h. The reaction mixture was kept stirring for additional 8 h at 0 °C. Then, deionized water (150 mL) was slowly added to the reaction mixture over a period of 6 h by a peristaltic pump. All the reaction processes were strictly controlled at 0 °C. The final reaction mixture was poured into ice-water mixture (1000 mL) to terminate the reaction, then hydrogen peroxide (30% aqueous solution) was added into the mixture under stirring until no gas escaped from the dispersion. The dispersion was filtrated and the filter cake was washed using diluted (3.7%) hydrochloric acid aqueous solution to remove the metal ions. The resultant slurry was then dispersed in distilled water under mild magnetic stirring to form a GO suspension. The GO suspension was purified by dialysis for two weeks. After that, it was centrifuged repeatedly at 3000 rpm to remove non-exfoliated aggregates. Finally, the GO suspension was concentrated by centrifugation at 10,000 rpm for 1 h. The concentration was evaluated to be at 7.40 mg mL^{-1} by weighting the dried solid from 1 mL concentrated GO dispersion.

GO_{35} was prepared by the oxidation of graphite powder (325 mesh, 3.0 g) following a modified Hummers' method. Briefly, graphite was added into the concentrated sulfuric acid (70 mL) under stirring at room temperature. Sodium nitrate (1.5 g) was added into the mixture and the reaction mixture was then cooled to 0 °C, followed by slowly adding potassium permanganate (9.0 g) under vigorous agitation to keep the temperature of the suspension lower than 20 °C. Then the reaction mixture was transferred to a 35-40 °C water bath for 30 min, successively, deionized water (150

mL) was added and reaction mixture was stirred for another 15 min at 90-95 °C. Deionized water (500 mL) was added into reaction mixture followed by the addition of hydrogen peroxide (30% aqueous solution, 20 mL). Finally, the dispersion was purified following the procedures for GO_0 preparation. The concentration of GO_{35} was evaluated to be at 7 mg mL^{-1}.

Supplementary Note 2 – Structural Characterization of GO Sheets

Scanning electron microscopy (SEM) images and the corresponding size distribution histograms demonstrate that GO_0 and GO_{35} sheets have an average lateral size of 12.5 and 13.5 μm, respectively (Figs. S1a, S1b, S1d, S1e). XPS surveys indicate that GO_0 sheets have a higher C/O ratio (2.29) than GO_{35} sheets (1.84), and the C 1s XPS peaks can be deconvoluted into five characteristic peaks, C=C (~284.7 eV), C–C (285.5 eV), C–OH/C–O–C (~286.7 eV), C=O (~287.6 eV) and HO–C=O (~289.2 eV) (Fig. S1c). The Raman spectra (Fig. S1f) display typical D- (1340 cm^{-1}) and G-band (1580 cm^{-1}) of GO, giving an I_D/I_G of 1.03 for GO_0 and 0.96 for GO_{35}, respectively. These results indicate that GO_0 and GO_{35} possess different chemical structures. GO_0 sheets prepared at low oxidation temperature of 0 ^oC have lower degree of oxidation, less defects and larger graphitic domains compared to GO_{35} sheets prepared by the conventional Hummer's method at the oxidation temperature of 35 °C.

Supplementary Note 3 – Mechanical Characterization

GO_{35} films show uniaxial tensile strength of 110 ± 22 MPa and strain to failure of 1.75 ± 0.26 %. Comparing with GO_{35} films, GO_0 films exhibit improved mechanical properties with tensile strength of 252 ± 16 MPa and strain to failure of 3.45 ± 0.51 %, with a benefit from the structural integrity of GO_0 precursors. Post-reduction of GO_0 films gave robust rGO_0 film with higher tensile strength (402 ± 18 MPa) and strain to failure (5.24 ± 0.12 %).

Supplementary Note 4 – Theoretical Model

Based on SEM and optical images of the cross-section and surface topography of CMG films (Figs. 4a-b), we constructed a schematic illustration of the microstructures for monolithic CMG films (Fig. 4c), which consists of an inter-connected network of CPLs (CMG multilayers with typical thickness of ~10-40 nm). With the structural features included in this model, one can establish quantitative understandings of the NPR effect. We consider a representative volume element (RVE) to capture the wavy texture of the inter-connected network of CPLs (Fig. 4d), where the orthotropic (solid, dash) sticks represent the disordered stacks, wrinkles, delamination of CPLs. The angle θ formed between the sticks and the basal plane of CMG films measures the amplitude of out-of-plane corrugation in CPLs, which can be related to the polarized Raman measurement of the alignment angle α. To correlate the value of NPRs with the alignment angle, the following assumption and analysis are made. Under a stretch force F on the CPL, the out-of-plane corrugation induced by disordered stacks, wrinkles and delamination will be reduced, resulting in extension in both tensile and lateral directions. In the tensile direction, this extension can be measured by displacements Δ_1 and Δ_2, that are

$$\Delta_1 = F\sin\theta s^3/3D,\ \Delta_2 = F\cos\theta s/K \tag{S1}$$

where D and K are the effective bending and tensile stiffness of the corrugated CPLs that are represented by sticks with a length of s.

The in-plane deformation of a RVE can be measured as

$$\Delta l = \Delta_1\sin\theta + \Delta_2\cos\theta,\ \Delta h = \Delta_2\sin\theta - \Delta_1\cos\theta \tag{S2}$$

As $w^2 = s^2 - h^2$, the change in the RVE width is $\Delta w = -h\Delta h/w = -\Delta h\tan\theta$, and thus the Poisson's ratio is

$$\nu_{YX} = -\frac{\Delta w / w}{\Delta l / l} = \frac{(1 - \frac{s^2 K}{3D}) \tan^2 \theta}{1 + \frac{s^2 K}{3D} \tan^2 \theta} \tag{S3}$$

by assuming $w = l$ with the assumption of in-plane isotropy in the CMG films. We also assume that $\tan\alpha$ is a linearly function of $\tan\theta$ with a pre-factor N ($\tan\theta = h/l = N\tan\alpha$).

Finally, denote $s^2K/3D$ as M, the Poisson's ratio can be expressed as

$$\nu_{YX} = \frac{(1 - M) N^2 \tan^2 \alpha}{1 + MN^2 \tan^2 \alpha} \tag{S4}$$

which is used to plot Fig. 4d.

Supplementary Figures and Captions

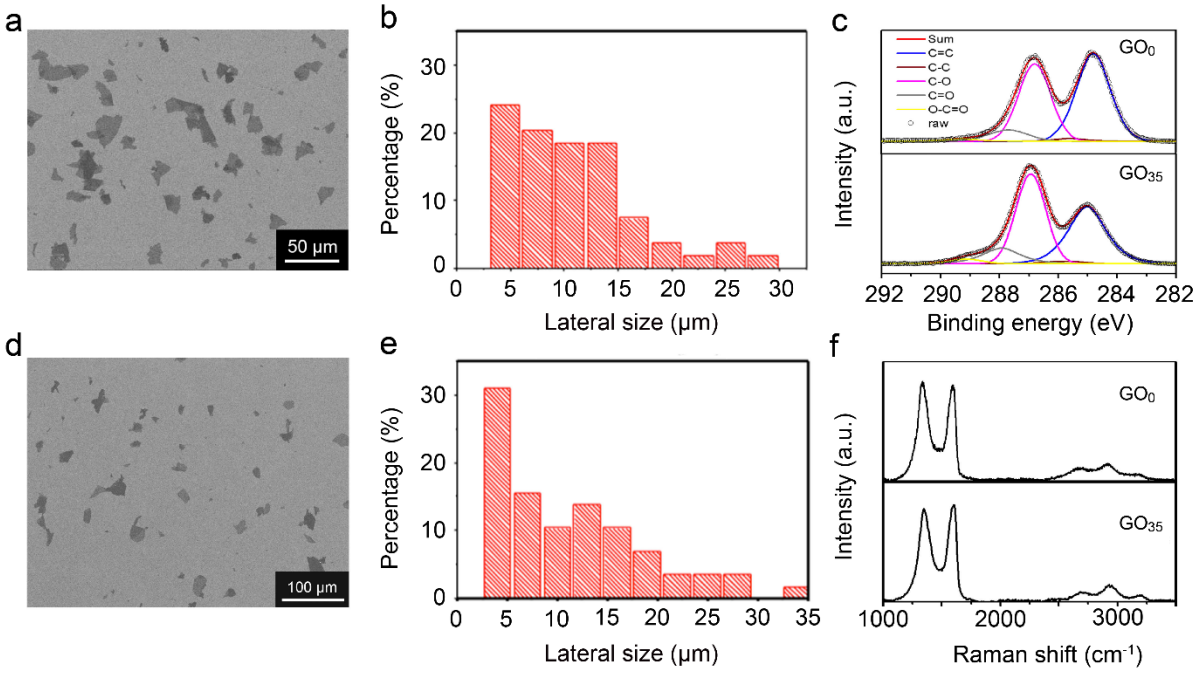

Supplementary Figure 1. Structural characterization of GO_0 and GO_{35} sheets. Scanning electron microscopy (SEM) images of GO_0 (**a**) and GO_{35} (**d**) sheets. The size-distribution histograms of GO_0 (**b**) and GO_{35} (**e**) measured from the SEM images. (**c, f**) XPS and Raman spectra of GO_0 and GO_{35} sheets. Source data are provided as a Source Data file.

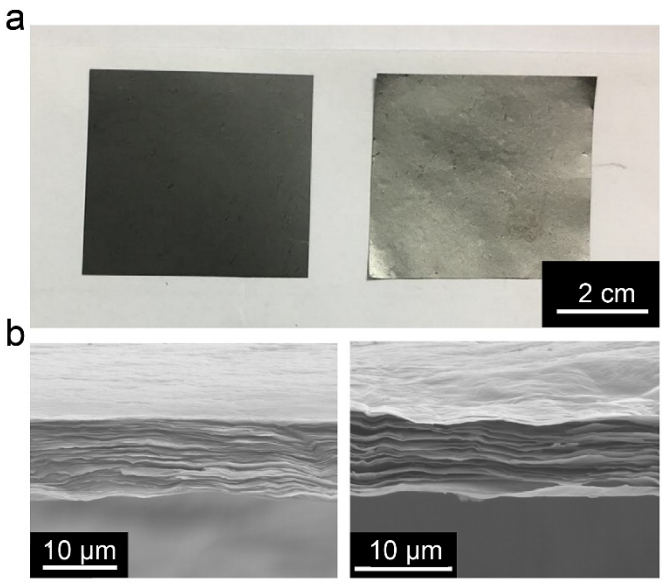

Supplementary Figure 2. CMG films and their SEM images. (a) Photographs of CMG (GO/left, rGO/right) films. Post-reduction of GO films gave rGO films with a metallic luster. (**b**) SEM cross-section images of the *e*-GO_0 (left) and *e*-rGO_0 (right) films, demonstrating the wavy textures of inter-connected network of CPLs in the CMG films.

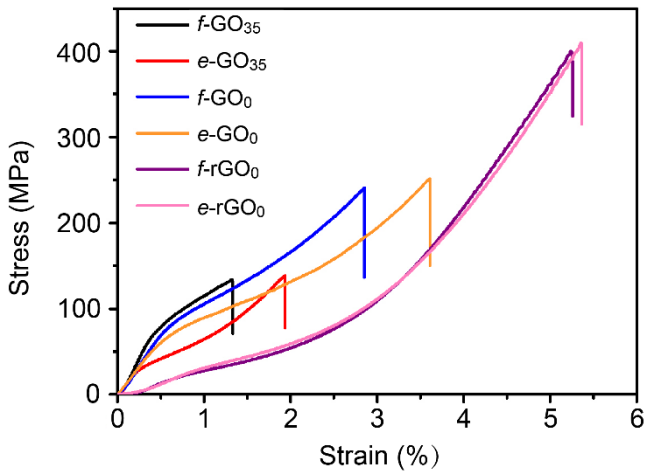

Supplementary Figure 3. Stress-strain curves of CMG films prepared from different GO precursors and film-forming methods. Source data are provided as a Source Data file.

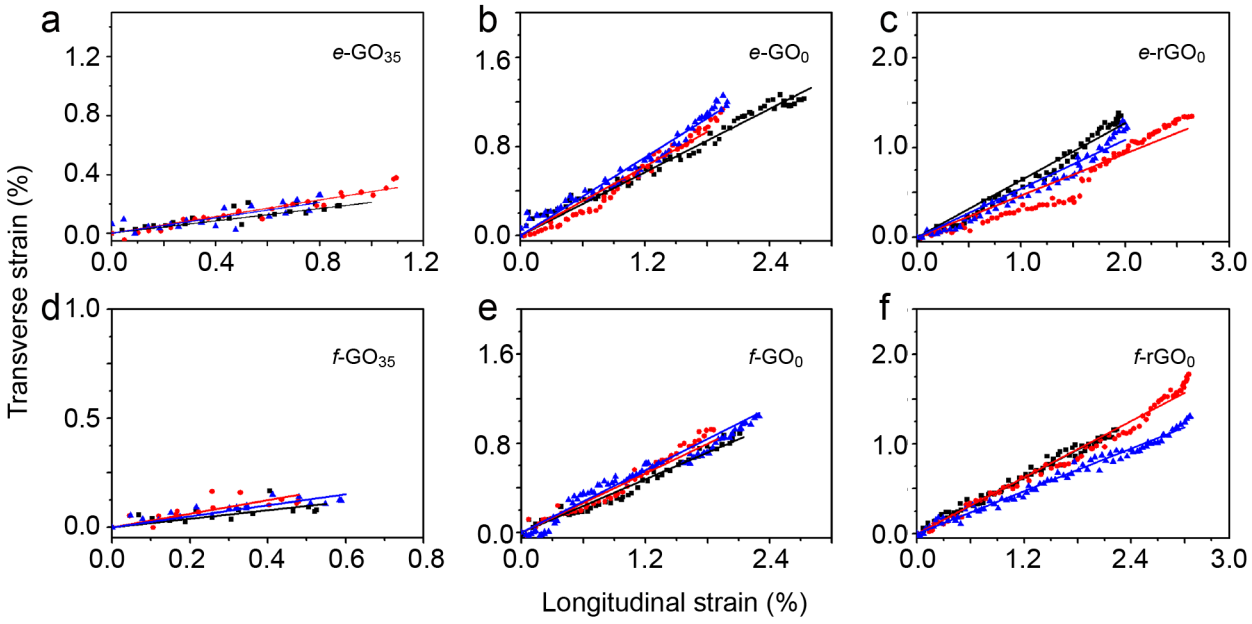

Supplementary Figure 4. Transverse strain plotted against the longitudinal strain applied to the CMG (GO or rGO) films. The average transverse strain of all samples (a, *e*-GO_{35}; b, *e*-GO_0; c, *e*-rGO_0; d, *f*-GO_{35}; e, *f*-GO_0; f, *f*-rGO_0) increases with the average longitudinal strain, demonstrating the NPR behavior. Source data are provided as a Source Data file.

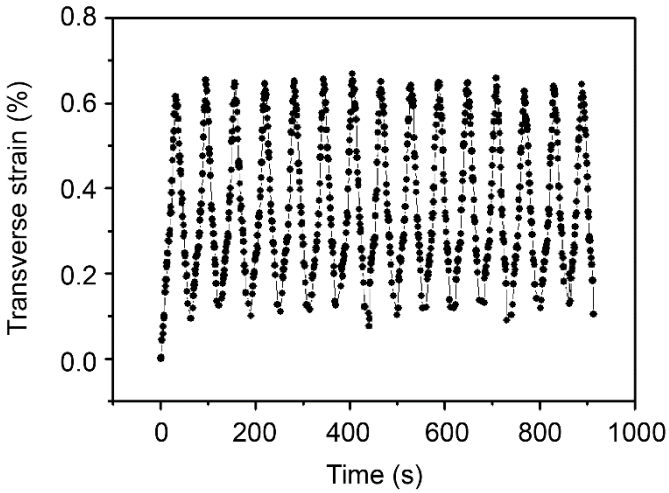

Supplementary Figure 5. Transverse strain plotted against time for *e*-GO_0 films under cyclic loading. The transverse strain is positive for the entire test, demonstrating the auxetic behavior of *e*-GO_0 films under cyclic loading-unloading tests with peak strain of 1.5%. Source data are provided as a Source Data file.

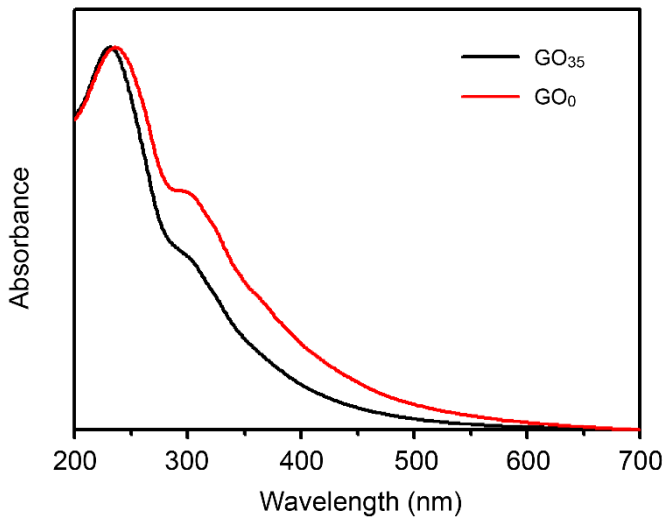

Supplementary Figure 6. UV-Vis absorption spectra of GO_0 and GO_{35} dispersions. The GO_0 sheets have a larger graphitic domain than that in GO_{35}. Source data are provided as a Source Data file.

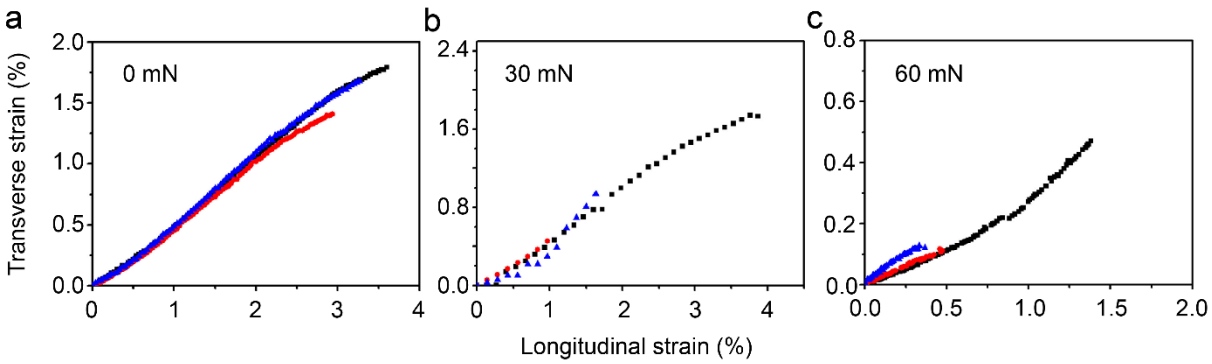

Supplementary Figure 7. Transverse strain plotted against the longitudinal strain for CMG films under pre-stretch of 0, 30 and 60 mN. The slope depends on the pre-stretch (0, 30 and 60 mN for panel a, b and c, respectively), indicating the tuned values of Poisson's ratios. Source data are provided as a Source Data file.

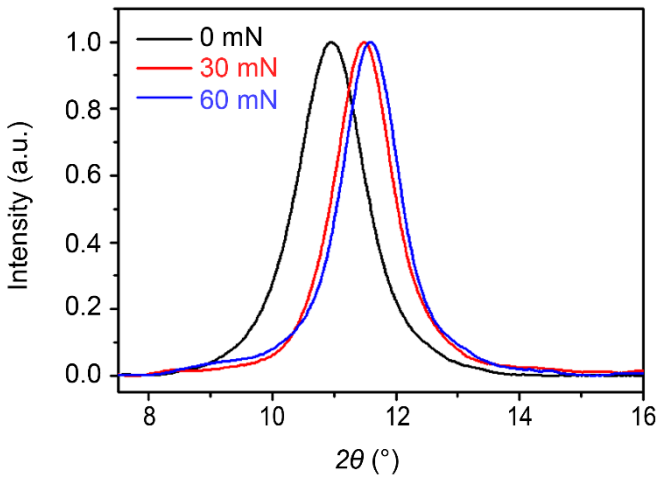

Supplementary Figure 8. XRD patterns of CMG films without and with pre-stretch (30 and 60 mN). Source data are provided as a Source Data file.

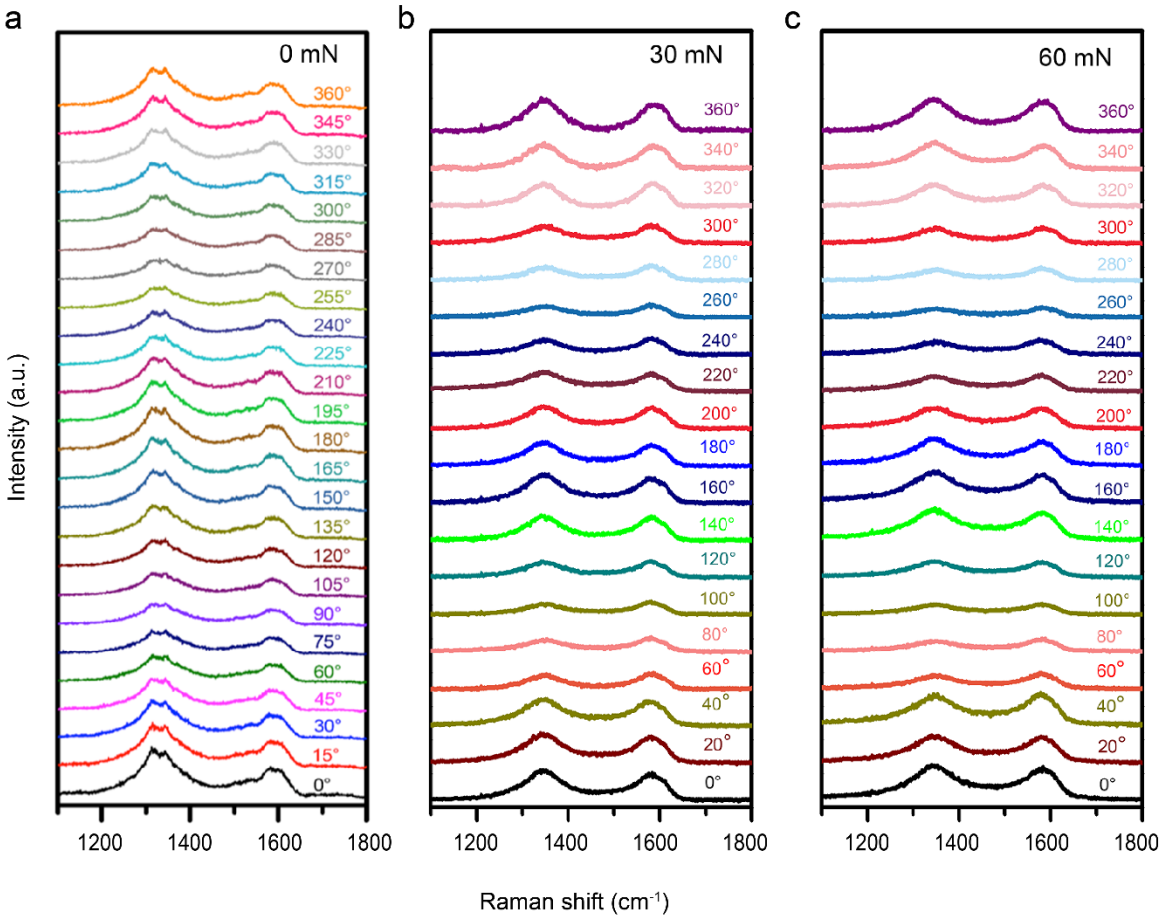

Supplementary Figure 9. Raman spectra for an *e*-GO_0 film under 0 (a), 30 (b) and 60 mN (c) pre-stretch. The *G*-band intensity in polarized Raman spectra of the *e*-GO_0 film changes with the angle β between the electric field vector of the incident laser and the base plane of the *e*-GO_0 film. Source data are provided as a Source Data file.